Swarthmore College

Works

Engineering Faculty Works

Engineering

8-1-1993

Internal stress wave measurements in solids subjected to lithotripter pulses

S. M. Gracewski

G. Dahake

Z. Ding

S. J. Burns

E. Carr Everbach
Swarthmore College, ceverba1@swarthmore.edu

Follow this and additional works at: https://works.swarthmore.edu/fac-engineering

Part of the Engineering Commons

Let us know how access to these works benefits you

Recommended Citation

Internal stress wave measurements in solids subjected to lithotripter pulses

S. M. Gracewski, Girish Dahake, and Zhong Ding
Department of Mechanical Engineering, University of Rochester, Rochester, New York 14627

S. J. Burns
Materials Science Program, Department of Mechanical Engineering, University of Rochester, Rochester, New York 14627

E. Carr Everbach
Electrical Engineering Department, University of Rochester, Rochester, New York 14627

Semiconductor strain gauges were used to measure the internal strain along the axes of spherical and disk plaster specimens when subjected to lithotripter shock pulses. The pulses were produced by one of two lithotripters. The first source generates spherically diverging shock waves of peak pressure approximately 1 MPa at the surface of the specimen. For this source, the incident and first reflected pressure (P) waves in both sphere and disk specimens were identified. In addition, waves reflected by the disk circumference were found to contribute significantly to the strain fields along the disk axis. Experimental results compared favorably to a ray theory analysis of a spherically diverging shock wave striking either concretion. For the sphere, pressure contours for the incident P wave and caustic lines were determined theoretically for an incident spherical shock wave. These caustic lines indicate the location of the highest stresses within the sphere and therefore the areas where damage may occur. Results were also presented for a second source that uses an ellipsoidal reflector to generate a 30-MPa focused shock wave, more closely approximating the wave fields of a clinical extracorporeal lithotripter.

PACS numbers: 43.80.Ev, 43.80.Sh

INTRODUCTION

Both cavitation and direct stress wave effects have been proposed as mechanisms that cause kidney stone and gallstone fragmentation during extracorporeal shock wave lithotripsy (ESWL).[1-4] A typical clinical lithotripter source produces a focused shock wave incident on the surface of a stone with a peak positive pressure of duration ~1 μs and magnitude ~100 MPa, followed or preceded by a tensile stress of lower magnitude but typically of longer duration. In addition, larger tensile stresses can develop within the stone as the compressive stress wave propagating in the stone material is reflected at the posterior stone surface. The cavitation hypothesis predicts that the rarefactional portion of the incident shock wave causes microbubbles present in the liquid surrounding the stone to expand and collapse violently near the stone surface.[2] Upon collapse, high localized stresses are produced that result in surface pitting and crack propagation that may ultimately fragment the stone. Alternatively, the direct stress wave hypothesis predicts damage on the anterior surface of a stone caused by compressive stresses and spalling of the posterior surface caused by tensile stresses generated within the stone.[1]

In stones with nonplanar boundaries, internal focusing effects may also occur. For example, a plane wave striking a sphere[5] or an explosion or point impact on the surface of a sphere[6,7] will result in caustics: lines along which linear theory predicts infinite stresses for a shock wave front. These caustics are for two extreme cases: the first is for a plane wave interacting with a sphere, that is, the source is far from the sphere; the second is for a diverging wave with the source on the surface of the sphere. The experiments studied in this paper are between these limits. The spherically diverging acoustic source is near enough to the targets so that curvature of the wave fronts is important. The location of the caustics is of interest since experimental studies have shown that fractures in Plexiglas spheres subjected to point explosive loading at the sphere surface occur initially at points where the caustics cross the symmetry axis.[6]

In vitro lithotripsy experiments have presented evidence for both the cavitation and direct stress wave mechanisms.[2-4,8-10] However, the relative importance of these mechanisms for stone fragmentation *in vivo* is still not well understood. A better understanding of the mechanisms involved in stone fragmentation and their dependence on lithotripter parameters such as pulse shape, duration, rise time, and peak positive or peak negative pressures may lead to improvements in lithotripter design or in more effective clinical procedures.

Knowledge of the evolution of stress fields inside concretions subjected to lithotripter pulses, along with measurements of the mechanical properties of the stones, may clarify failure processes. In this paper, we describe a technique of implanting silicon strain gauges within plaster samples to obtain information about these internal stress fields. Test specimens of simple geometries (i.e., disks and spheres) have been chosen for this study so that the reflec-

tions from the boundaries can be more easily identified and compared with theoretical models. Experimental results are obtained for both spherically diverging and focused shock wave sources. Theoretical models based on geometrical acoustics are presented for a spherical wave front incident on a disk and on a sphere. The caustic surfaces for a spherically diverging wave incident on a sphere are presented. Finally, predictions from these models are compared with the experimental results.

I. EXPERIMENTAL METHODS

A. Strain gauge characteristics and sample preparation

Monocrystalline silicon semiconductor strain gauges (UFP-500-060, Kulite Semiconductor Products, Inc., Leonia, NJ) were chosen because of their high sensitivity and small size. Their gauge factor ($140 \pm 5\%$ at 24° C) is two orders of magnitude larger than conventional metallic wire strain gauges. The silicon gauges are U shaped with a half-width of 0.2 mm and an effective gauge length of 0.8 mm. These silicon gauges, like conventional wire gauges, are intended to be long and slender, so that corrections for transverse strains are small. The longitudinal and shear wave speeds of the gauge material are $c_d^g = 8930$ m/s and $c_s^g = 5320$ m/s, respectively, as calculated from published data for the density (2331 kg/m^3), Young's modulus (161 GPa), and Poisson's ratio (0.225) of silicon.[11] The frequency response of the gauge is primarily limited by the relationship between the gauge length and the wavelength of the lithotripter pulse and by the amplifying circuit bandwidth. For instance, the pulse length in the gauge for a longitudinal wave of 1-μs duration is 9 mm, so the pulse length is nine times the effective length of the gauge. In the surrounding plaster, the pulse length would be 3 mm. Because the total change in resistance of the gauge will be proportional to the average strain along the length of the gauge, the shock rise time and peak value will not be represented accurately. However, information about the arrival times, relative magnitudes, and polarity of the strain wave pulses can be obtained from the strain gauges.

A strain gauge produces a change in resistance when subjected to a stress or strain. The lead wires of the gauge are attached to an electronic circuit that converts the change in resistance to a change in voltage and amplifies the signal. The output signal is displayed on a LeCroy model 9400 digital oscilloscope and transferred to a computer for plotting and analysis. Electromagnetic noise from the spark sources is minimized by using short coaxial cables and by electrically shielding the electronics and the strain gauge.

Spherical and disk-shaped specimens were fabricated by pouring a plaster mixture, 100 parts Ultracal 30 (United States Gypsum Company, Chicago, IL) to 36 parts water by weight, into Plexiglas molds and allowing the plaster to set. These molds were designed so that a strain gauge, glued to a 10-μm-diam. fiber of Kevlar™ (DuPont Corp., Wilmington, DE), could be positioned within the mold before the plaster was poured. Minimal amounts of glue were used to bond the gauges to the fibers and unbacked gauges were used to enhance the bonding between each gauge and the plaster. For the experiments described in this paper, a gauge was positioned at the center of each of the specimens, and in the disk, the gauge was aligned with the axis.

The plaster spheres were 2.25 cm in diameter. The plaster disks were 10.2 cm in diameter and approximately 3 cm thick. Before each experiment, the plaster samples were submerged in degassed water and degassed under a 24-in. Hg vacuum for at least 1 h. Samples were then pressurized at 10 atm for approximately 45 min to drive any remaining air bubbles into solution.

B. Wave speed and density measurements of plaster

The longitudinal and shear wave speeds and the density of the plaster are required for the theoretical analysis. The wave speeds were calculated from the propagation times in 1- and 0.5-cm-thick plaster samples that were degassed as described above. The samples were cut with a diamond saw to obtain parallel faces. Half-inch diameter 2.25-MHz longitudinal wave and 1-MHz shear wave transducer pairs were used (Panametrics, Inc., Waltham, MA). Transmit and receive transducers were coupled directly to the sample's surfaces. The measurements on eight samples were averaged. The measured value for the longitudinal wave speed c_d is 3290 ± 40 m/s and for the shear wave speed c_s is 1750 ± 90 m/s (mean $\pm$ standard deviation).

The specific gravity S_g for three degassed plaster samples was calculated from measurements of their weight in air W_a and their weight in water W_w as $S_g = W_a / (W_a - W_w)$. Their specific gravity was found to be 1.88 ± 0.01.

C. Experimental setup for strain measurements

Two lithotripters were used in this study. The first, a Wolf model 2137.50 Electrohydraulic Lithotripter (Richard Wolf GMBH, Postfach 4D, D-7134 Knittlingen, Germany), generates spherically diverging shock waves by producing an underwater spark at the end of a 3-mm coaxial cable (9F probe). With each spark, a bubble is created that expands and collapses twice before it shatters into microbubbles. A shock wave is generated with the creation of the initial bubble and upon each collapse. Campbell et al.[12] describe the details of the bubble behavior and characterize the resulting shock waves fields. They report that the standard deviation of the spark-to-spark peak positive pressure variation is on the order of 20%. There is negligible rarefactional pressure. The positive pressure amplitude of each shock wave pulse as it propagates in degassed water is inversely proportional to the radial distance from the shock source. The time history of the pressure, measured at 9 cm from the source by a Marconi (Marconi Research Center, Chelmsford, England) bilaminar PVDF membrane hydrophone with a 1.0-mm-diam. sensitive element, is shown in Fig. 1. At this distance from the shock source, the amplitude of the first shock wave pulse (see insert) is about 1 MPa. The second pulse
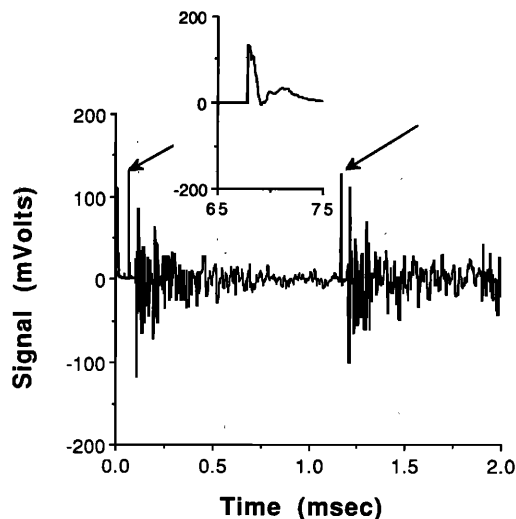
FIG. 1. Signal from a membrane hydrophone positioned 9 cm from a Wolf electrohydraulic lithotripter. The first two acoustic shock waves arriving at the hydrophone, indicated by the arrows, are of comparable amplitude. Each acoustic pulse is followed by noise generated as the waves reflect off the hydrophone mount.[12] The insert, with time axis in μs, shows the first acoustic pulse in more detail.

arrives approximately 1 ms later. For the experiments presented here, times were chosen so that only the effects of this first shock wave striking the sample as measured by the strain gauges were recorded. Similar results were also obtained for the second shock wave. The Wolf source was used in most of our experiments because of the simplicity in modeling the spherically diverging waves.

The second lithotripter used in this study was designed by Coleman[13] as a low-cost experimental lithotripter that would facilitate the examination of acoustic fields in ESWL. The shock wave source and measured waveforms are similar to those of the clinical Dornier HM3 lithotripter. The shock waves, generated by spark discharge under water, are focused by a brass ellipsoidal reflector. The focal diameter is 1 cm with a peak positive pressure of about 30 MPa. The Coleman lithotripter was used to observe the strain fields in plaster disks subjected to fields more typical of clinical ESWL.

Samples were always positioned so that the strain gauges were along the axis of symmetry of the lithotripters, thereby aligning each strain gauge with a principal direction of strain. For the Wolf lithotripter, the samples were aligned using a three-way positioner so that their front surface was either 9 or 15 cm from the shock source. For the Coleman lithotriper, they were positioned so that their front surface was at the lithotripter focus.

Two masks could be placed between the Wolf source and a disk sample to partially block the incident wave. Mask A consisted of a 5-mm-thick aluminum plate with a 5.1-cm-diam. hole at its center, covered with a 1.4-mm-thick corprene layer containing a 4.2-cm-diam. hole, concentric with that of the plate. Corprene is a corklike material that will prevent the acoustic waves that strike it from propagating to the sample. This mask was positioned so that the direct wave could reach the strain gauge. The

mask was large enough, however, to block any waves that would have reached the outer rim of the disk. Mask B consisted of a 1.3-cm-diam., 1-cm-thick piece of Plexiglas covered with a 0.5-mm-thick layer of corprene. This mask was positioned to block the direct wave incident on the strain gauge, but allow waves to reach the outer rim of the disk. Masks were not aligned with the strain gauge axis so that edge diffraction effects would be minimized. No masks were used with the Coleman lithotripter because, for this focused wave, the energy reaching the outer rim of the disk is negligible.

II. GEOMETRICAL ACOUSTICS

Ray theory is used to approximate the wave propagation and reflections within the samples for the shock waves generated by the Wolf lithotripter. These shock waves are only weakly nonlinear, so linear theory is likely to provide a good approximation over short propagation distances. The plaster material is assumed to be homogeneous, isotropic, and linear elastic. The coupling water is assumed to be inviscid and to extend to infinity so acoustic reflections from the liquid boundary can be neglected. Absorption and scattering will contribute to additional attentuation of the waves within the samples, but are neglected since experimental values are not available. The models, discussed below, are axisymmetric and geometrical acoustics is used to predict the arrival times and approximate amplitudes of internally reflected waves arriving at the strain gauges. The location of the caustics, pressure contours of the incident pressure wave, and wave fronts at various times are also determined for the sphere. Because the number of reflected waves arriving at the strain gauge rapidly becomes large as time increases, the analysis for the disk is carried out for 50 μs after the arrival of the direct pulse. The reflection coefficients, needed to calculate the amplitudes and phases of reflected and refracted waves, are summarized in the Appendix.

For the following analyses, the displacement vector $\mathbf{u}$ in the solid is expressed in terms of the scalar potential ϕ and the vector potential ψ in the form

$$\mathbf{u} = \nabla\phi + \nabla\times\psi, \tag{1}$$

where ϕ and ψ satisfy the wave equations

$$\nabla^2\phi = \frac{1}{c_d^2}\frac{\partial^2\phi}{\partial t^2}, \quad c_d^2 = \frac{\lambda+2\mu}{\rho},$$

$$\nabla^2\psi = \frac{1}{c_s^2}\frac{\partial^2\psi}{\partial t^2}, \quad \nabla\cdot\psi = 0, \quad c_s^2 = \frac{\mu}{\rho}, \tag{2}$$

with λ and μ denoting the Lamé constants and ρ the density of the solid. In the liquid, the displacement vector $\mathbf{u}_l$ is expressed in terms of the scalar potential ϕ_l that satisfies the wave equation

$$\nabla^2\phi_l = \frac{1}{c_l^2}\frac{\partial^2\phi_l}{\partial t^2}, \quad c_l^2 = \frac{k_l}{\rho_l}, \tag{3}$$

with k_l and ρ_l denoting the bulk modulus and the density of the liquid, respectively.
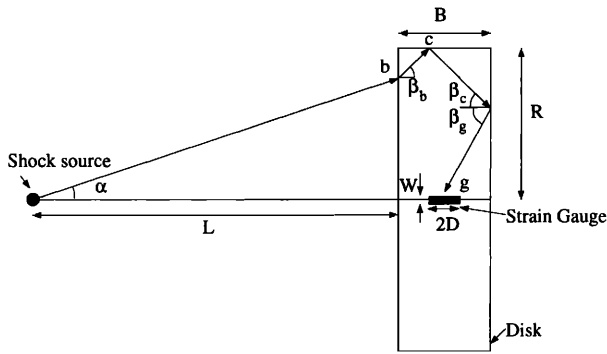
FIG. 2. Propagation path of a ray generated at a point shock source that reflects off the circumference of a solid disk and strikes the center of a strain gauge aligned with the disk axis.

A. Disk

A diagram of a disk of radius R and thickness B, at a distance L from the shock source is shown in Fig. 2. A strain gauge of length $2D$ and width W is aligned with the central axis and positioned at the center of the disk. In addition to the wave that propagates from the source directly to the strain gauge, oblique waves can also be reflected by the circumference of the disk so that they strike the gauge. The ray path at an angle α from the axis is shown for a wave incident on the front of the disk. The path b, c, g ultimately strikes the center of the gauge. Only the pressure (P) waves generated at each reflection or refraction are shown. However, shear (S) waves are also produced resulting in 2^{N+2} wave fronts, where N is the number of reflections by either face of the disk. For the ray path in the figure, $N=1$.

We have considered all possible combinations for $N \leqslant 3$ for which the wave front arrives at the strain gauge less than 50 μs after the direct wave does. These combinations can be represented in terms of the five cases presented in Table I. The case label represents the wave type. For example, PPS^nP^mS represents a P wave striking the disk circumference generating a reflected P wave followed by n S waves and m P waves reflected from either the front or back surfaces and then an S wave that ultimately strikes the strain gauge. In Table I, the time t for the wave to reach the strain gauge is given in terms of the incident angle α and the angles β_d and β_s that the P and S waves, respectively, make with the normal to the front surface of the disk. These angles are determined from Snell's law and the geometric relation given in Table I for each case. The plus or minus signs ($\pm$) correspond to waves striking the edges of the gauge that are farthest or nearest to the source, respectively.

The change in amplitude of a wave propagating along a ray can be estimated by assuming that in a narrow tube of rays the energy remains constant, unless a boundary is encountered. At a boundary, the amplitude is modified by the appropriate reflection or transmission coefficient. Ignoring the curvature of the wave front at the strain gauge and making use of the assertion that the reflection and transmission coefficients at an interface are independent of

TABLE I. Relations for waves reflecting from the circumference of the disk.

Case	Arrival time and geometric relation
PSS^n	$t = \dfrac{L}{c_l \cos \alpha} + \dfrac{R}{c_s \sin \beta_s} + \dfrac{R - L \tan \alpha}{c_d \sin \beta_d}$
	$R(\cot \beta_d + \cot \beta_s) = L \tan \alpha \cot \beta_d + (n + \tfrac{1}{2}) B \pm D$
PPS^nP^mP	$t = \dfrac{L}{c_l \cos \alpha} + \dfrac{(m + 1.5) B \pm D}{c_d \cos \beta_d} + \dfrac{nB}{c_s \cos \beta_s}$
	$2R = L \tan \alpha + nB \tan \beta_s + [(m + 1.5) B \pm D] \tan \beta_d$
PPS^nP^mS	$t = \dfrac{L}{c_l \cos \alpha} + \dfrac{(m + 1) B}{c_d \cos \beta_d} + \dfrac{(n + 0.5) B \pm D}{c_s \cos \beta_s}$
	$2R = L \tan \alpha + [(n + 0.5) B \pm D] \tan \beta_s$
	$\qquad + (m + 1) B \tan \beta_d$
SSP^nS^mS	$t = \dfrac{L}{c_l \cos \alpha} + \dfrac{nB}{c_d \cos \beta_d} + \dfrac{(m + 1.5) B \pm D}{c_s \cos \beta_s}$
	$2R = L \tan \alpha + nB \tan \beta_d + [(m + 1.5) B \pm D] \tan \beta_s$
SSP^nS^mP	$t = \dfrac{L}{c_l \cos \alpha} + \dfrac{(m + 1) B}{c_s \cos \beta_s} + \dfrac{(n + 0.5) B \pm D}{c_d \cos \beta_d}$
	$2R = L \tan \alpha + [(n + 0.5) B \pm D] \tan \beta_d$
	$\qquad + (m + 1) B \tan \beta_s$

the curvatures of the incident wave front and the interface,[5] the energy density E_g at the strain gauge can be expressed as

$$\frac{E_g}{E_0} = A^* T_b(\alpha) R_c \left(\frac{\pi}{2} - \beta_b \right) \prod_{k=1}^{N} R_k(\beta_{k-1}). \qquad (4)$$

In this expression, T_b is the power transmission coefficient for the wave incident from the liquid into the solid, R_c is the power reflection coefficient for the wave incident on the circumference, R_k is the power reflection coefficient of the kth reflection on the disk front or back face. The power reflection (transmission) coefficients are obtained by squaring the appropriate potential amplitude coefficient listed in the Appendix and multiplying by the ratio of the reflected (transmitted) wave speed to the incident wave speed. Also, β_k is defined as the reflected angle for the kth interaction with the front or back surfaces, with $\beta_0 = \beta_c$. The value of $E_0 \sim 5 \times 10^{-3}$ MPa m³/s was obtained by fitting measurements of the energy density of the spherically diverging source wave to the form

$$E = E_0 / \bar{r}^2, \qquad (5)$$

where $\bar{r}$ is the distance from the source.

The geometric factor in Eq. (4) is given by

$$A^* = \left(\frac{\cos \alpha}{L} \right)^2 \frac{r_b' s_b'}{r_c s_c} \frac{r_c' s_c'}{r_g s_g} \prod_{k=1}^{N} \frac{r_k' s_k'}{r_k s_k}, \qquad (6)$$

where r and s are the two principle radii of curvature and the unprimed and primed quantities correspond to radii of curvature before and after reflection or transmission, respectively. The subscripts c and g indicate the locations where the ray intersects the circumference and strain gauge, respectively, and subscript b indicates the location

that the incident wave first strikes disk. Subscript k indicates the location of the kth interaction with the front or back surfaces.

The radii of curvature, with positive magnitude for the convex wave front, are given by

$$r_b' = \frac{\cos\beta_b}{[\tan(\beta_b)/\tan(\alpha)][\cos^2(\alpha)/L]}, \quad s_b' = \frac{L\tan\alpha}{\sin\beta_b},$$
$$(7)$$

$$r_c = r_b' + \frac{R - L\tan\alpha}{\sin\beta_b}, \quad s_c = \frac{R}{\sin\beta_b}, \quad (8)$$

$$r_c' = \frac{\cos\beta_c}{[\tan(\beta_c)/\tan(\beta_b)][\cos(\beta_b)/r_c]}, \quad s_c' = \frac{R}{\sin\beta_c},$$
$$(9)$$

$$r_1 = r_c' + \frac{B - (R - L\tan\alpha)/\tan\beta_b}{\cos\beta_c}, \quad s_1 = \frac{d_1}{\sin\beta_c},$$
$$(10)$$

$$d_1 = R - \left(B - \frac{R - L\tan\alpha}{\tan\beta_b}\right)\tan\beta_c,$$

$$r_k = r_{k-1}' + \frac{B}{\cos\beta_{k-1}}, \quad s_k = \frac{d_k}{\sin\beta_{k-1}},$$
$$(11)$$

$$d_k = d_{k-1} - B\tan\beta_{k-1},$$

$$r_k' = \frac{\cos\beta_k}{[\tan(\beta_k)/\tan(\beta_{k-1})][\cos(\beta_{k-1})/r_k]},$$
$$(12)$$

$$s_k' = \frac{d_k}{\sin\beta_k},$$

$$r_g = r_N' + \frac{B}{2\cos\beta_N}, \quad s_g = \frac{W}{2\sin\beta_N}, \quad \text{if } N > 0,$$
$$(13)$$

$$r_g = r_c' + \frac{R - W/2}{\sin\beta_c}, \quad s_g = \frac{W}{2\sin\beta_N}, \quad \text{if } N = 0.$$

The waves are axially symmetric so the s curvature tends to zero as the wave front approaches the axis of symmetry. Since the strain gauge, located along this axis, actually has finite width W, a relative measure of the various wave amplitudes is obtained by calculating the strain in the gauge direction at a distance $W/2$ from the axis of symmetry.

The normal strain along the length of the gauge is then, for P waves,

$$e_{zz} = (E_g/\rho c_d^3)^{0.5}\cos^2\beta_d, \quad (14)$$

and, for S waves,

$$e_{zz} = (E_g/\rho c_s^3)^{0.5}\sin(\beta_s)\cos(\beta_s). \quad (15)$$

The theoretical predictions for peak amplitude are shown superimposed above experimental results in Fig. 3. For an S wave incident on an interface, it is possible that the P wave is inhomogeneous and therefore, the resulting reflection coefficient for the S wave will be complex. In this case, the waveform will change shape upon reflection and the prediction, shown as a dashed line, is only an estimate of the peak strain. These theoretical predictions match well
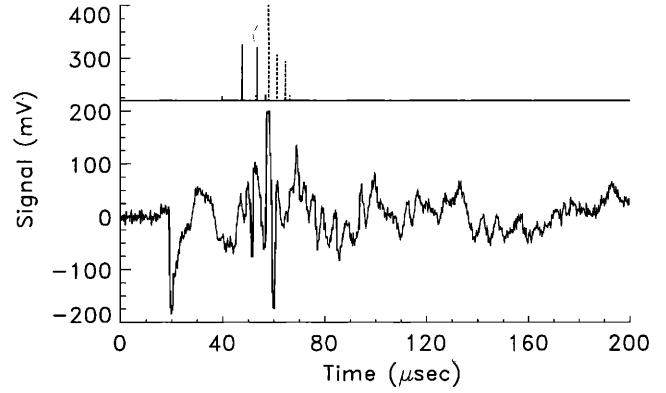

FIG. 3. Ray theory predictions of strain amplitude versus time for waves reflected by the circumference of a disk with its front surface 9 cm from a spherically diverging shock wave source, superimposed above the experimentally measured strain gauge response. The wave types contributing to the theoretical predictions are, from left to right, *PP*, *PPS*, *SSP*, *PS*, *PPSP*, *PSS* (*SSPS* and *PPSS*), *PSSS*, and *SSPPS*. Dashed lines are used to indicate waves that experience a change in shape upon reflection from the circumference of the disk.

with arrival times of the largest experimental peaks that, as discussed in the next section, have been identified as reflections from the disk circumference.

B. Sphere

A spherically diverging pressure wave in a liquid incident on a solid sphere will create a complicated wave pattern within the sphere. Initially, the incident wave will refract at the solid surface generating longitudinal and shear wave fronts that propagate across the sphere. Because the wave fronts are curved, the amplitude of the waves will decrease as they propagate away from the source. When these waves reach the posterior sphere boundary, a portion of the energy will be reflected back into the sphere. These reflected waves will be convergent because of the curvature of the surface of the sphere. For each reflected wave front, ray theory predicts a caustic line, along which the amplitude of the wave is infinite for an incident shock wave. The complexity of the resulting wave fields increases rapidly with time, since with each reflection two waves, a longitudinal and a shear wave, are created, each propagating at a different speed. In the following, wave fronts as a function of time, caustics, and pressure contours of the incident pressure wave will be presented.

Consider a point shock wave source a distance L from the nearest surface of a sphere of radius a. Ray tracing will be used to determine the position of the wave front as a function of time.[5,14] Ray AB originates at the source A, with angle θ_1 to the horizontal axis as shown in Fig. 4. The angle θ between this ray and the normal to the sphere at B is given by the solution to the equation

$$\{L + a[1 - \cos(\theta - \theta_1)]\}\tan\theta_1 = a\sin(\theta - \theta_1). \quad (16)$$

In terms of these angles, the coordinates of B, using the coordinate system in Fig. 4, can be written as

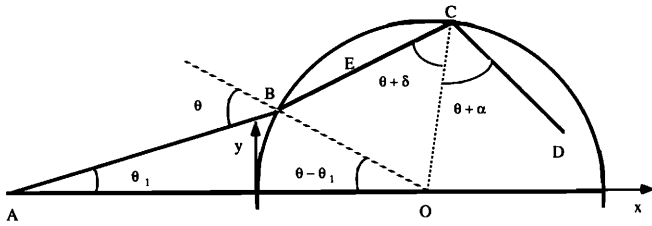$$x_B = a[1 - \cos(\theta - \theta_1)], \quad y_B = a\sin(\theta - \theta_1), \quad (17)$$

FIG. 4. Refraction and reflection of an incident ray inside a solid sphere. A is the wave source. The wave is refracted at B and propagates inside the sphere with a reflection at C. AO is the axis of symmetry.

FIG. 5. Longitudinal wave fronts at times $\Delta t = 0.1, 0.3, 0.5, 0.7, 0.9, 1.0$, and $1.1\ \mu s$ in a 2.2-cm-diam. solid sphere with its front surface 9 cm from a spherically diverging shock wave source. Arrows indicate the direction of propagation of the wave fronts. The inflection points lie along the PP caustic in Fig. 6.

with the wave front reaching B at time t_B given by

$$t_B = (L + x_B)/(c_l \cos \theta_1). \tag{18}$$

The ray will be refracted inside the sphere such that ray BC will make an angle $\theta + \delta$ with the normal to the sphere at B. The angle δ is determined by Snell's law:

$$(1/c_i)\sin(\theta + \delta) = (1/c_l)\sin \theta, \tag{19}$$

where $i = d$ or s for a refracted longitudinal or shear wave, respectively. The position of any point E along BC at time t can be expressed as

$$\begin{aligned} x_E &= x_B + (t - t_B)c_i \cos(\theta_1 + \delta), \\ y_E &= y_B + (t - t_B)c_i \sin(\theta_1 + \delta), \end{aligned} \tag{20}$$

for $t_B < t < t_C$, where

$$t_C = t_B + 2a \cos(\theta + \delta)/c_i. \tag{21}$$

The coordinates of point C are obtained by setting $t = t_C$ in Eq. (20).

Similarly, the position of any point D on the wave front after reflection inside the sphere is given by

$$\begin{aligned} x_D &= x_C - (t - t_C)c_j \cos(2\theta + \theta_1 + 2\delta + \alpha), \\ y_D &= y_C - (t - t_C)c_j \sin(2\theta + \theta_1 + 2\delta + \alpha), \end{aligned} \tag{22}$$

for $t_C < t < t^*$, where t^* is the time this ray crosses the symmetry axis and is given by

$$t^* = \frac{a \sin(\theta + \theta_1 + 2\delta)}{c_j \sin(2\theta + \theta_1 + 2\delta + \alpha)}. \tag{23}$$

The reflected wave makes an angle $\theta + \alpha$ with the normal to the sphere at C, with α determined by Snell's law:

$$(1/c_i)\sin(\theta + \delta) = (1/c_j)\sin(\theta + \alpha), \tag{24}$$

where $j = d$ or s for a reflected longitudinal or shear wave, respectively.

The longitudinal wave fronts for a spherically diverging wave incident on the sphere are shown in Fig. 5 for various values of time. In this figure, $\Delta t = t - L/c_l$ is time measured from when the wave first touches the sphere. Because of symmetry, only the upper half of the sphere is shown. The wave diverges as it propagates toward the back surface of the sphere and after reflection from this surface, converges to a point along the axis of symmetry. There are points of inflection at the intersections of the reflected and forward propagating portions of the wave fronts. These
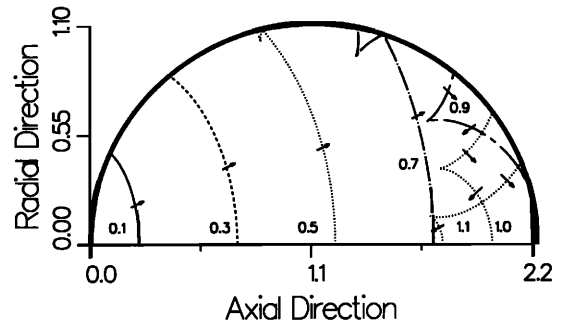
inflection points lie on the curve that defines the caustic discussed below. Similar plots can also be obtained for the shear wave fronts. These will lag behind the longitudinal wave fronts due to the slower wave speed. In addition, there will be mode conversion upon reflection of the waves from the back surface of the sphere, generating two more sets of reflected wave fronts and, therefore, four caustics will be generated.

The caustics are defined by the points in Fig. 4 at which the radius of curvature of the wave front vanishes. By extending the analysis of Ref. 15 to include possible mode conversion at interfaces, we obtained expressions for the caustics:

$$\begin{aligned} x_D &= x_C - \overline{CD} \cos(2\theta + \theta_1 + 2\delta + \alpha), \\ y_D &= y_C - \overline{CD} \sin(2\theta + \theta_1 + 2\delta + \alpha), \end{aligned} \tag{25}$$

where $\overline{CD}$ is given by

$$\overline{CD} = \frac{aH \cos(\theta + \alpha)}{H + c_j \sin \theta/(c_i \cos(\theta + \alpha)\tan \theta_1)}, \tag{26}$$

with

$$H = 1 + \left(2\frac{c_i \cos \theta}{c_l \cos(\theta + \delta)} - 1\right)\frac{\tan \theta}{\tan \theta_1}. \tag{27}$$
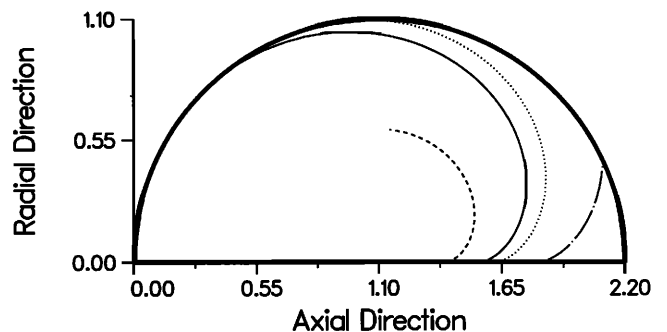
Caustics are shown in Fig. 6 for a spherically diverging

FIG. 6. Caustics of the PP (solid), SS (dotted), PS (dashed), and SP (dot–dashed) wave fronts in a solid sphere with its front surface 9 cm from a spherically diverging shock wave source.

shock wave striking a sphere. There are four caustics, corresponding to the purely longitudinal wave (*PP*), to the purely shear wave (*SS*), and to the waves that undergo mode conversion upon reflection from the back surface of the sphere (*PS* and *SP*).

The pressure contours of the longitudinal wave, as it propagates from the front to the back surface of the sphere, can also be determined by wave front analysis. Let ξ_1, ξ_2, and ξ_3 be a system of orthogonal coordinates with ξ_1 normal to the wave front. The stone and water are initially at rest so the region ahead of the longitudinal wave front is undisturbed, therefore the only nonvanishing component of strain immediately behind the wave front is ϵ_{11}. The pressure p defined as the average of the normal compressive stresses can then be written as

$$p = -(\lambda + \tfrac{2}{3}\mu)\epsilon_{11} = -(\lambda + \tfrac{2}{3}\mu)\nabla^2\phi. \tag{28}$$

Consider the potential amplitude ϕ_d^B of the refracted longitudinal wave at point B on the sphere interface (Fig. 4) due to an incident wave with amplitude ϕ_0^B in the liquid. The plane wave reflection coefficients listed in the Appendix can be used to obtain the amplitude ratios and

$$\frac{p_B}{p_l} = \frac{\rho(c_d^2 - \tfrac{4}{3}c_s^2)}{\rho_l c_d^2} \frac{\phi_d^B}{\phi_0^B}. \tag{29}$$

The energy density integrated across a tube of rays remains constant in the sphere resulting in the equation

$$p^2 rs = \text{const}, \tag{30}$$

where r and s are the principal radii of curvature of the wave front. The radii of curvature r_B and s_B of the wave front just inside the sphere at a point B are given by

$$r_B = \cos(\theta + \delta) \left[\frac{\tan(\theta + \delta)}{\tan\theta} \left(\frac{\cos\theta}{r_l} + \frac{1}{a} \right) - \frac{1}{a} \right]^{-1},$$
$$\tag{31}$$
$$s_B = (a\sin\theta)/(\sin\delta),$$

where r_l is the radius of curvature of the wave front in the liquid at point B, given by $r_l = L/\cos\theta_1$. The radii of curvature r_E and s_E at an arbitrary point E along BC can be expressed as

$$r_E = r_B + \overline{BE}, \quad s_E = s_B + \overline{BE}. \tag{32}$$

Finally, the pressure at point E given in terms of the above expressions is

$$\frac{p_E}{p_l} = \frac{p_B}{p_l} \left(\frac{r_B s_B}{r_E s_E} \right)^{0.5}. \tag{33}$$

The pressure in the liquid at point B is given by $p_l = p_0 \cos\theta_1/L$, where p_0 depends on the magnitude of the source. For the Wolf lithotripter, $p_0 \approx 9$ MPa cm.

Relative pressure contours for the spherically diverging wave impinging on a sphere are shown in Fig. 7. These contours can be used to predict the pressure amplitude of the first pulse propagating across the strain gauge.
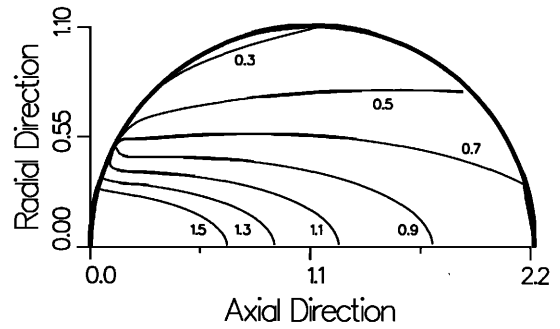

FIG. 7. Pressure contours of the longitudinal wave front in a solid sphere with its front surface 9 cm from a spherically diverging shock wave source.

III. EXPERIMENTAL RESULTS

A. Disk

The electronic response versus time plots for two excitations of a strain gauge imbedded in a disk that was positioned 15 cm from a Wolf electrohydraulic lithotripter are shown in Fig. 8. All data plotted for the plaster disks were obtained from a strain gauge located at the center of the disk along the axis as shown in Fig. 2. The two response curves in Fig. 8 were chosen for comparison since the amplitudes of the direct wave were similar, indicating that these resulted from similar initial shock wave amplitudes. A 60-μs time delay, used in all plots except where indicated, ensured that the acoustic signal of interest was recorded on the oscilloscope screen. The arrival time of the first pulse varied by up to 10 μs because of variations in triggering. Therefore, all time measurements have been referenced to the time of the direct shock pulse. As seen from Fig. 8, the spark-to-spark reproducibility was good. The strain gauge signal is initially negative indicating compression. The first pulse arriving at the strain gauge was the direct compression wave that strikes the center of the disk. A larger signal that was surrounded by other compressive and tensile pulses was observed approximately 40 μs after the first pulse. After the series of experiments shown in
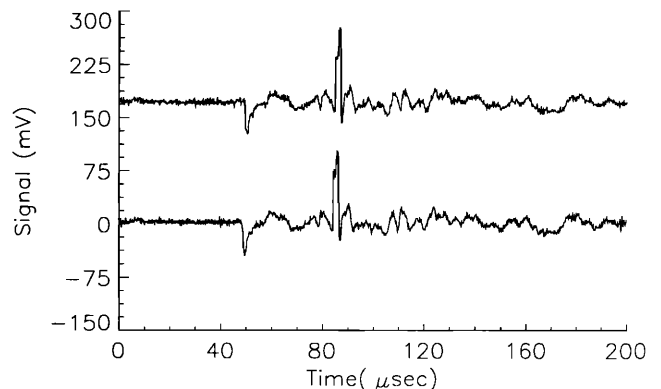

FIG. 8. Strain gauge response versus time for a disk positioned with its front surface 15 cm from a Wolf electrohydraulic lithotripter. The two traces correspond to two different incident waves and show the good reproducibility of the signal. The upper trace was offset vertically so that the traces would not overlap.
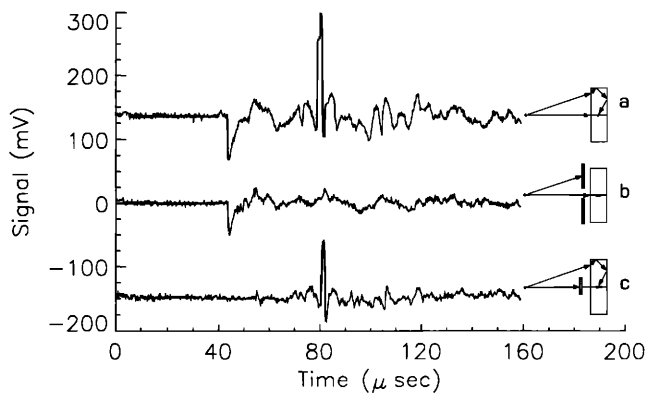
FIG. 9. Strain gauge response versus time for a disk positioned with its front surface 15 cm from a Wolf electrohydraulic lithotripter, with (a) no mask, (b) mask A, and (c) mask B placed between the source and the disk. Traces (a) and (c) have been shifted vertically.
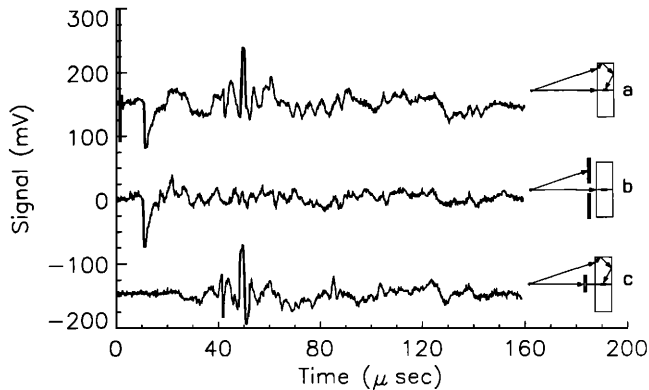
FIG. 10. Strain gauge response versus time for a disk positioned with its front surface 9 cm from a Wolf electrohydraulic lithotripter, with (a) no mask, (b) mask A, and (c) mask B placed between the source and the disk. Traces (a) and (c) have been shifted vertically.

Fig. 9 and described below, these larger signals were identified as reflections from the circumference of the disk. Only the first 50 μs after the initial pulse arrival was analyzed, because after this point the signal to noise ratio is too low to consistently identify features of the response. Also, after this time the interval between waves predicted by the theory becomes too short to distinguish individual pulses.

Traces (a), (b), and (c) of Fig. 9 show the response of a strain gauge imbedded in a disk that was again positioned 15 cm from the lithotripter. These are three consecutive signals so the spark-to-spark variation in incident shock wave is evident and not accounted for. For the top trace, no mask was used and therefore the response resembles the traces in Fig. 8. For the middle trace, mask A was placed between the Wolf source and the disk to block the waves incident on the circumference of the disk, but allowing the direct wave to reach the strain gauge. In this trace, the large signal occurring approximately 40 μs after the arrival of the direct wave has been suppressed by the mask. For the bottom trace, mask B was placed between the Wolf source and the disk to block the wave propagating directly toward the strain gauge. Therefore, in this trace, the initial compressive pulse and the tensile pulse due to its reflection from the back surface have been suppressed.

Figure 10 shows the strain gauge response to a sequence of experiments identical to those in Fig. 9, except that the disk was positioned with its front surface only 9 cm from the spark source. The arrival time of the direct pulse was therefore 40 μs earlier and the amplitude was larger because of the shorter propagation distance in the water. The features of the response are similar to those in Fig. 9, although additional waves reflected by the disk circumference are evident.

Figure 11 shows the response of the strain gauge when the disk was placed with its front surface at the focal point of the Coleman lithotripter. A delay of 180 μs was used in this case because of the longer water propagation path to the focus. The amplitude of the first pulse for the Coleman lithotripter is an order of magnitude larger than for the Wolf lithotripter, as expected. The width of the first pulse

is approximately 5 μs, a factor of approximately 2 greater than the incident shock wave as measured in water by a PVDF needle hydrophone (Imotec, Wurselen, Germany).[16] After the initial pulse, the response is approximately periodic with an average peak-to-peak period of 19 μs.

B. Sphere

Figure 12 shows the two response curves for a strain gauge imbedded in the center of a sphere placed 9 cm from the Wolf spark source, with the gauge aligned along the axis of symmetry. These two curves indicate the good spark-to-spark reproducibility of the response. The initial compression peak is due to the direct wave. The largest tensile pulse, following 7.7 ± 1 μs later, is the wave reflected by the back surface of the sphere. The amplitude of this tensile peak is larger than the incident compressive peak because of focusing effects. Other peaks surrounding the largest tensile pulse result from the S wave (arriving before the largest tensile peak) and the PS and SP waves (arriving after the largest tensile peak). The long term response is a decaying oscillation with an average peak-to-
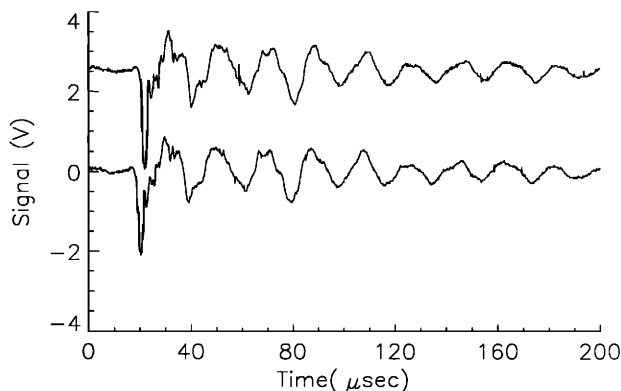

FIG. 11. Strain gauge response versus time for a disk positioned with its front surface at the focus of the Coleman lithotripter. The two traces correspond to two different incident waves, with the upper trace offset vertically.

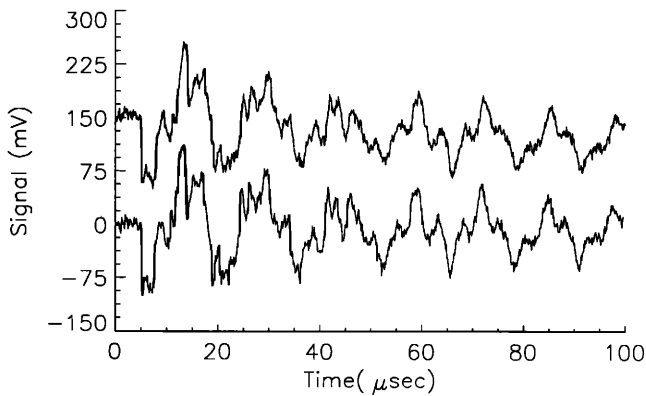Gracewski *et al.*: Stress measurements of lithotripter pulses

FIG. 12. Strain gauge response versus time for a sphere positioned with its front surface 9 cm from a Wolf electrohydraulic lithotripter. The two traces correspond to two different incident waves, with the upper trace offset vertically so that the traces would not overlap.

peak period of approximately 14 μs. A lower bound for an oscillation period would be that for a longitudinal wave propagating back and forth along the axis.[17] Twice the sphere diameter divided by the measured longitudinal wave speed gives an oscillation period of 13.4 μs. Similar results were also obtained for another similarly fabricated sphere, indicating good gauge-to-gauge reproducibility.

IV. DISCUSSION

We have shown that semiconductor silicon strain gauges can be used to determine the wave fields inside plaster samples. The incident and reflected pressure waves can readily be identified for both the disk and sphere. In addition, the incident and reflected shear waves are also evident for the sphere. In the disk, larger peaks following the initial direct pulse were identified as waves reflecting off of the circumference of the disk and being focused to the central axis.

In the presentation of results, only relative amplitudes of the stress waves were compared. To obtain an estimate of the magnitudes of the waves, the change in resistance of the strain gauge needs to be related to the stresses within the gauge and plaster matrix. Because the magnitudes of stress in the present experiment are within the linear range of the gauges, the change in resistance of the gauge ΔR_g can be expressed either in terms of the stress σ_g or the strain ϵ_g along the gauge as

$$\Delta R_g / R_{g0} = \pi_g \sigma_g = GF \epsilon_g, \tag{34}$$

where R_{g0} is the initial resistance along the axis of a strain gauge and π_g and GF are proportionality constants that depend on the stress state and gauge construction.

The stress state in the gauge is complicated not only because the gauge is imbedded in the plaster, but also because a nonhomogeneous stress state is generated by a wave with wavelength on the order of the gauge length. Since the gauge is along the axis of symmetry, the shear stresses in the gauge coordinates are assumed to be zero. The direct waves propagating in a straight line from the source to the gauge are assumed to strike the end of the

gauge and propagate along its length. For this situation, the gauge is assumed to be much stiffer than the matrix, such that the lateral stresses can be neglected. Under these assumptions, the only nonzero stress will be σ_g along the gauge and the manufacturer's gauge factor $GF = 140$ can be used. For the circuit gain of 150 used in these experiments, the above analysis predicts a change in voltage of 100 mV for $\sigma_g = 1$ MPa.

The amplitude of the initial compressive pulse in the disk at a distance of 15 cm from the Wolf spark source was ~50 mV. Based on the above analysis, this corresponds to a stress of 0.5 MPa. The peak stress in the plaster along the axis at the center of the disk is ~1.5 MPa. A uniform stress of this magnitude would result in a 150-mV signal. However, since the gauge is of a finite length, the peak response would correspond to an average and not the peak pressure along the gauge and would therefore be lower than this estimate. The good correlation between the expected and the measured responses indicates that the strain gauges are functioning close to their design specifications even though they are imbedded in the plaster.

In this paper, we have shown that imbedded semiconductor strain gauges can be used to monitor the internal stress waves in plaster disks and spheres subjected to lithotripter pulses. In the future, we plan to use these gauges to monitor the variation of maximum stress with experimental conditions, such as sample position, size, shape, and mechanical properties, coupling liquid viscosity and gas content, and lithotripter type and settings. The strain gauges can also be used to locate the regions of maximum stress and to determine whether this maximum stress is correlated with a region of initial or maximum stone damage.

ACKNOWLEDGMENTS

APPENDIX: REFLECTION AND TRANSMISSION COEFFICIENTS

The reflection and transmission coefficients used in this paper are listed in this Appendix in terms of the nondimensional quantities $\hat{\rho} = \rho / \rho_l$, $\hat{c}_d = c_d / c_l$, and $\hat{c}_s = c_s / c_l$. All coefficients are for plane waves incident on a planar liquid–solid boundary with the solid occupying the domain $x_2 < 0$ and the liquid occupying $x_2 > 0$. That plane wave reflection and transmission coefficients can be used even for nonplanar shock wave fronts incident on nonplanar interfaces is demonstrated theoretically in Refs. 5 and 15 and supported by experimental evidence for high-frequency acoustic waves in Ref. 18. The angles between the normal to the interface and propagation direction of the P wave in the liquid and the P and S waves in the solid are denoted

by β_l, β_d, and β_s, respectively. The particle displacement vector for the shear wave is rotated 90° clockwise from the propagation direction.

The reflection coefficients for a P wave with propagation vector $\mathbf{p}_0 = \sin\beta_d \hat{i} + \cos\beta_d \hat{j}$ incident from the solid are given by

$$\frac{\psi_s}{\phi_0} = -\frac{2\hat{\rho}}{D} \frac{\hat{c}_s}{\hat{c}_d} \cos\beta_l \cos(2\beta_s)\sin(2\beta_d) \tag{A1}$$

and

$$\frac{\phi_d}{\phi_0} = 1 + \frac{\hat{c}_d^2}{\hat{c}_s^2} \frac{\cos(2\beta_s)}{\sin(2\beta_d)} \frac{\psi_s}{\phi_0}. \tag{A2}$$

The reflection coefficients for an S wave with propagation vector $\mathbf{p}_0 = \sin\beta_s \hat{i} + \cos\beta_s \hat{j}$ incident from the solid are given by

$$\frac{\phi_d}{\psi_0} = \frac{\hat{\rho}}{D} \frac{\hat{c}_d}{\hat{c}_s} \cos\beta_l \sin(4\beta_s) \tag{A3}$$

and

$$\frac{\psi_s}{\psi_0} = -1 + \frac{\hat{c}_s^2}{\hat{c}_d^2} \frac{\sin(2\beta_d)}{\cos(2\beta_s)} \frac{\phi_d}{\phi_0}. \tag{A4}$$

The transmission coefficients for a P wave with propagation vector $\mathbf{p}_0 = \sin\beta_l \hat{i} - \cos\beta_l \hat{j}$ incident from the liquid are given by

$$\frac{\phi_d}{\phi_0} = \frac{2}{D} \frac{\hat{c}_d}{\hat{c}_s} \cos\beta_l \cos(2\beta_s) \tag{A5}$$

and

$$\frac{\phi_s}{\phi_0} = \frac{2}{D} \frac{\hat{c}_s}{\hat{c}_d} \cos\beta_l \sin(2\beta_d). \tag{A6}$$

The denominator D in these expressions is given by

$$D = \hat{\rho}\cos\beta_l \left(\frac{\hat{c}_d}{\hat{c}_s} \cos^2(2\beta_s) + \frac{\hat{c}_s}{\hat{c}_d} \sin(2\beta_s)\sin(2\beta_d) \right)$$
$$+ \frac{\cos\beta_d}{\hat{c}_s}. \tag{A7}$$

[1] C. Chaussy, W. Brendel, and E. Schmiedt, "Extracorporeally induced destruction of kidney stones by shock waves," Lancet **20**, 1265–1268 (1980).

[2] A. J. Coleman, J. E. Saunders, L. A. Crum, and M. Dyson, "Acoustic cavitation generated by an extracorporeal shockwave lithotripter," Ultrasound Med. Biol. **13**, 69–76 (1987).

[3] M. Delius, "Effect of lithotripter shock waves on tissues and materials," in *Frontiers of Nonlinear Acoustics: Proceedings of 12th ISNA*, edited by M. F. Hamilton and D. T. Blackstock (Elsevier, London, 1990), pp. 31–46.

[4] W. Sass, M. Bräunlich, H.-P. Dreyer, E. Matura, W. Folberth, H.-G. Priesmeyer, and J. Seifert, "The mechanisms of stone disintegration by shock waves," Ultrasound Med. Biol. **17**, 239–243 (1991).

[5] T. C. T. Ting and E. H. Lee, "Wave-front analysis in composite materials," J. Appl. Mech. **36**, 497–504 (1969).

[6] J. F. Silva-Gomes, S. T. S. Al-Hassani, and W. Johnson, "A note on times to fracture in solid perspex spheres due to point explosive loading," Int. J. Mech. Sci. **18**, 543–545 (1976).

[7] H.-H. Gildemeister and K. Schönert, "Berechnung zur wellenausbreitung in kugeln und bruchphänomene in kreisscheiben bei prallbeanspruchung," in *3rd European Symposium on Comminution* (Weinheim/Bergstrasse, Verlag Chemie, 1971), pp. 199–233.

[8] N. Vakil, S. M. Gracewski, and E. C. Everbach, "Relationship of model stone properties to fragmentation mechanisms during lithotripsy," J. Litho. Stone Disease **3**, 304–310 (1991).

[9] J. P. Whelan and B. Finlayson, "An experimental model for the systematic investigation of stone fracture by extracorporeal shock wave lithotripsy," J. Urol. **140**, 395–400 (1988).

[10] J. Rassweiler, A. Westhauser, P. Bub, and F. Eisenberger, "Second-generation lithotripters: a comparative study," J. Endourol. **2**, 193–204 (1988).

[11] H. M. Ledbetter, "Elastic Properties," in *Materials at Low Temperatures*, edited by R. P. Reed and A. F. Clark (American Society for Metals, Metals Park, OH, 1983), pp. 8 and 9.

[12] D. S. Campbell, H. G. Flynn, D. T. Blackstock, C. Linke, and E. L. Carstensen, "The acoustic fields of the Wolf electrohydraulic lithotripter," J. Litho. Stone Disease **3**, 147–156 (1991).

[13] A. J. Coleman, J. E. Saunders, and M. J. Choi, "An experimental shock wave generator for lithotripsy studies," Phys. Med. Biol. **34**, 1733–1742 (1989).

[14] F. G. Friedlander, *Sound Pulses* (Cambridge U.P., Cambridge, 1958).

[15] J. D. Achenbach, J. H. Hemann, and F. Ziegler, "Separation at the interface of a circular inclusion and the surrounding medium under an incident compressive wave," J. Appl. Mech. **37**, 298–304 (1970).

[16] The calibration rise time for the Imotec hydrophone was 80–100 ns (10%–90%). See Ref. 7 for a discussion of the response of the Imotec and Marconi hydrophones to Wolf lithotripter shock wave pulses.

[17] A. E. H. Love, *A Treatise on the Mathematical Theory of Elasticity* (Dover, New York, 1944), pp. 278–286.

[18] K. L. Williams and P. L. Marston, "Mixed-mode acoustical glory scattering from a large elastic sphere: Model and experimental verification," J. Acoust. Soc. Am. **76**, 1555–1563 (1984).